

# CONDITIONAL DIFFUSION WITH ORDINAL REGRESSION: LONGITUDINAL DATA GENERATION FOR NEURODEGENERATIVE DISEASE STUDIES

**Anonymous authors**

Paper under double-blind review

## ABSTRACT

Modeling the progression of neurodegenerative diseases such as Alzheimer’s disease (AD) is crucial for early detection and prevention given their irreversible nature. However, scarcity of longitudinal data and complex disease dynamics make the analysis highly challenging. Moreover, longitudinal samples often contain irregular and large intervals between subject visits, which underscore the necessity for advanced data generation techniques that can accurately simulate disease progression over time. In this regime, we propose a novel conditional generative model for synthesizing longitudinal sequences and present its application to neurodegenerative disease data generation conditioned on multiple time-dependent ordinal factors, such as age and disease severity. Our method sequentially generates continuous data by bridging gaps between sparse data points with a diffusion model, ensuring a realistic representation of disease progression. The synthetic data are curated to integrate both cohort-level and individual-specific characteristics, where the cohort-level representations are modeled with an ordinal regression to capture longitudinally monotonic behavior. Extensive experiments on four AD biomarkers validate the superiority of our method over nine baseline approaches, highlighting its potential to be applied to a variety of longitudinal data generation.

## 1 INTRODUCTION

**Motivation & Background.** Modeling progressive changes in the brain is vital for early diagnosis of neurodegenerative diseases and effective treatment planning (Paulsen et al., 2013). However, the task is highly challenging due to the scarcity of samples. That is, the data are collected from longitudinal visits from individuals over a long period, and they become significantly limited and imbalanced due to increased mortality as the disease worsens. Moreover, it requires sophisticated neuroimaging techniques such as positron emission tomography (PET) and magnetic resonance imaging (MRI) to observe the progression *in-vivo*, which are expensive in cost, labor and time, and often involve exposure to high radiation level (Hosono et al., 2021), aggravating the data scarcity problem.

Several neuroimaging initiatives such as ADNI (Mueller et al., 2005), OASIS (LaMontagne et al., 2019) and WRAP (Johnson et al., 2018) try to tackle this problem by collecting data from a large cohort over a decade with several follow-up visits from individual subjects. They consist of a population of sequences of samples that provides information on *longitudinal* disease trajectories. Previous longitudinal studies have yielded successful results such as predicting the future evolution of individuals at risk of AD (Marinescu et al., 2018) and imputing missing outcomes within trajectories (Luo et al., 2016) by fully exploiting the dataset when sufficient sample size became available.

Alternatively, rather than waiting for individuals to be affected by neurodegeneration, one may utilize generative methods to obtain real-like synthetic longitudinal samples. Conditional generative models (Hwang et al., 2019; Yang et al., 2021) have shown promising results in creating sequential data from scratch using time-varying diagnostic labels as conditions. However, these methods overlook the prior information of the condition which can be critical such as the irreversible nature of neurodegeneration. Moreover, these methods do not consider discontinuities in sample points caused by long intervals between clinical assessments (often ranging from 6 months to 6 years) (Mueller et al., 2005), and this inconsistency is a major practical issue in longitudinal disease analyses.

**Proposed method.** To address the issues discussed above, we propose **Conditional Diffusion** model using **Ordinal Regression** (ConDOR), which generates long-term sequences conditioned on various ordinal factors. In this work, ConDOR is specifically applied to model the progression of degenerative disorders by synthesizing brain regional measurements based on disease-relevant metadata, such as age and sequential diagnostic labels that describe disease progression. These factors, which change monotonically over time (e.g., increasing age and deteriorating labels), serve as conditions to characterize disease trajectories and generate realistic brain measurements from imaging scans.

Specifically, ConDOR operates as an autoregressive model, sequentially generating samples from baseline to follow-up time points with a diffusion model to address the temporal heterogeneity among subjects. To tackle data discontinuities caused by long intervals between collections, ConDOR gradually generates unobserved interim samples, conditioned on interpolated ages and labels between consecutively observed time points. These pseudo-samples are crafted as a combination of two components: *cohort-level* and *subject-level* samples. A cohort-level sample is modeled with an ordinal regression (Winship & Mare, 1984) fitted to the entire population to explicitly learn the globally common transition pattern in ordinal factors. On the other hand, individual variability is incorporated as a subject-level sample obtained by interpolating samples in consecutive visits, which captures characteristics unique to individuals with aging and various disease manifestation patterns. Ultimately, these cohort and subject-level samples are combined to form unobserved interim pseudo-samples, and ConDOR iteratively estimates the difference in these consecutive pseudo-samples to reconstruct the subsequent observation at the next time point. Such concept of separately modeling *consistent* group-level and *variational* sample-level features has been traditionally studied in machine learning and computer vision, e.g., face recognition models that integrate common face with personal traits (Becerra-Riera et al., 2019; Yan et al., 2022) and graph models that aggregate features from global semantic clusters and local node similarities (Xu et al., 2021; Kuang et al., 2019).

Furthermore, to address the limited sample-size issues in medical data, we introduce an extended framework of ConDOR that learns data from multiple datasets by using an additional domain condition. This approach maximizes the utility of available data from diverse sources, thus enhancing the model’s robustness and applicability. By flexibly utilizing both time-dependent (i.e., age and label) and time-independent conditions (i.e., domain), ConDOR can be potentially applied not only to various medical data but also to other data types where data are scattered over various sites, making it a versatile model for a wide range of applications.

**Contributions.** Our contributions are summarized as follows. **1)** We propose a novel generative model for longitudinal data, conditioned on ordinal factors such as age and disease severity. By incorporating ordinal regression into a diffusion model, our method effectively captures the ordinality of conditions. **2)** To handle temporal heterogeneity within visits, our method sequentially generates samples that seamlessly fill gaps within sparse data points. These interim samples capture both population-level trends and individual-specific features by a dual-sampling approach, which leads to generating personalized longitudinal data. **3)** To maximize the utility of limited data, the framework is extended to enable the model to learn data from different sources with a domain condition. By integrating both time-invariant and time-dependent factors, ConDOR improves generalizability across diverse datasets while capturing common progressive features.

As a result, ConDOR demonstrates its generality and efficacy on four independent AD biomarkers, provided by Alzheimer’s Disease Neuroimaging Initiative (ADNI) and Open Access Series of Imaging Studies (OASIS). Also, ConDOR yields interpretable results at the brain regional level, validating that the generated results characterize realistic AD progression.

## 2 METHOD

In this section, we introduce “ConDOR”, a method for generating sample sequences with time-varying ordinal conditions. We first introduce the details of the task that we aim to solve and the way of sampling from a conditional density function using Bayes’ Theorem and ordinal regression, which forms the cornerstones of our model. Subsequently, we explain how the sampling strategy is integrated into a diffusion model, and further describe an extended version for learning data from multiple sources.

### 2.1 PROBLEM DEFINITION: DATA GENERATION WITH ORDINAL CONDITIONS

Consider a longitudinal sequence of samples  $\{\mathbf{x}_t\}_{t=1}^T$ , where the samples for  $t = 1, \dots, T$  time points ( $T \geq 2$ ) are presented in chronological order. Each sample  $\mathbf{x}_t \in \mathbb{R}^B$  represents a set of

independent features at time  $t$ , e.g., a set of brain measurements obtained from  $B$  brain regions of interest (ROIs). For each time point, the samples come with ordinal conditions, e.g., age  $\{a_t\}_{t=1}^T$  and diagnostic labels  $\{y_t\}_{t=1}^T$  within a disease spectrum, where  $y_t \in \{1, \dots, C\}$  denotes the disease progression from the healthy control state ( $y_t = 1$ ) to the most deteriorated state ( $y_t = C$ ).

This study aims to characterize the progressive disease patterns and generate longitudinal sequences that comply with the ordinal conditions. Assuming that the brain regional measurements  $\mathbf{x}_t$  as realizations of a random vector  $\mathbf{X} = [X_1, \dots, X_B]$  and age  $a_t$  and disease stage  $y_t$  are realizations of random variables  $A$  and  $Y$  respectively, a sample distribution is defined as  $\mathbf{x}_t \sim f_{\mathbf{X}|A,Y}(\mathbf{x}_t|a_t, y_t)$ . Here, the  $f_{\mathbf{X}|A,Y}(\mathbf{x}_t|a_t, y_t)$  is a conditional probability density function (PDF) indicating the distribution of brain measurements for given age and disease stage. This formulation allows us to simulate realistic progression scenarios by considering both age and disease-specific variations in the brain.

## 2.2 REFINING CONDITIONAL PDF WITH BAYES' THEOREM

Using Bayes' Theorem (Bayes, 1763), the conditional PDF  $f_{\mathbf{X}|A,Y}(\mathbf{x}_t|a_t, y_t)$  is formulated as

$$f_{\mathbf{X}|A,Y}(\mathbf{x}_t|a_t, y_t) = \frac{p_{Y|\mathbf{X},A}(y_t|\mathbf{x}_t, a_t) \cdot f_{\mathbf{X}|A}(\mathbf{x}_t|a_t)}{p_{Y|A}(y_t|a_t)}, \quad (1)$$

which enables the decomposition of the complex, high-dimensional distribution into interpretable components. The first term  $p_{Y|\mathbf{X},A}(y_t|\mathbf{x}_t, a_t)$  represents a probability mass function (PMF) that a subject is at a disease stage  $y_t$  for given brain measurements and age. Given that  $y_t$  is a discrete and ordinal variable, the PMF can be effectively modeled using an ordinal regression (Winship & Mare, 1984) to capture its ordinal nature. The second term  $f_{\mathbf{X}|A}(\mathbf{x}_t|a_t)$  is a prior distribution characterizing age-relevant effects in estimating  $\mathbf{x}_t$ . As we do not assume any shape such as ordinality for  $\mathbf{x}_t$ , it needs to be directly estimated from given data using a non-parametric method such as kernel density estimation (KDE) (Parzen, 1962). Lastly, the denominator  $p_{Y|A}(y_t|a_t) \triangleq \Pr(Y = y_t|A = a_t)$  represents the probability of being at stage  $y_t$  given age  $a_t$ , which serves as a scaling constant. In the following sections, we introduce detailed methods of modeling  $p_{Y|\mathbf{X},A}(y_t|\mathbf{x}_t, a_t)$  and  $f_{\mathbf{X}|A}(\mathbf{x}_t|a_t)$  to estimate the conditional PDF  $f_{\mathbf{X}|A,Y}(\mathbf{x}_t|a_t, y_t)$  and describe the sampling process of  $\mathbf{x}_t$  from the estimated PDF using inverse transform sampling (Devroye, 1986).

**Modeling  $p_{Y|\mathbf{X},A}(y_t|\mathbf{x}_t, a_t)$  with ordinal regression.** As  $Y$  denotes discrete ordinal categories that describe the natural degenerative progression of a disease (i.e., healthy to disease), the distribution  $p_{Y|\mathbf{X},A}(y_t|\mathbf{x}_t, a_t) \triangleq \Pr(Y = y_t|\mathbf{X} = \mathbf{x}_t, A = a_t)$  can be effectively estimated using an ordinal regression model. Unlike nominal classifiers that treat all labels independently, the ordinal regression accounts for the ordered nature of ranked groups, ensuring that gradual transitions in disease stages are captured. This approach leads to more accurate predictions and meaningful interpretations, as the model explicitly considers that the difference between non-adjacent stages (e.g., healthy vs. disease) is more significant than the difference between adjacent stages (e.g., healthy vs. prodromal). Also, since brain measurements  $\mathbf{X}$  are key biomarkers that reflect the disease progression (Counts et al., 2017) and age  $A$  is a risk factor of neurodegenerative diseases (Brown et al., 2005), using such factors as features of an ordinal regression enables effective estimation of the disease stage  $Y$ .

Given the ordered categories  $y_t \in \{1, \dots, C\}$ , the probability of being at or below a certain stage  $y_t$  is computed using cumulative probabilities as follows

$$\Pr(Y \leq y_t | \mathbf{X} = \mathbf{x}_t, A = a_t) = \Phi(\tau_{y_t} - \beta_{\mathbf{X}}^T \mathbf{x}_t - \beta_A^T a_t), \quad (2)$$

where  $\Phi(\cdot)$  is the logistic function defined as  $\Phi(x) = \frac{1}{1 + \exp(-x)}$  and  $\beta$ 's are regression coefficients. The parameter  $\tau_{y_t}$  is a threshold that separates the  $y_t$ -th stage from the next  $(y_t + 1)$ -th stage, satisfying  $\tau_1 < \tau_2 < \dots < \tau_{C-1}$ . The above equation further allows us to derive the probability of being at the stage  $y_t$  by taking the difference between consecutive cumulative probabilities as

$$\Pr(Y = y_t | \mathbf{X} = \mathbf{x}_t, A = a_t) = \Phi(\tau_{y_t} - \beta_{\mathbf{X}}^T \mathbf{x}_t - \beta_A^T a_t) - \Phi(\tau_{y_t-1} - \beta_{\mathbf{X}}^T \mathbf{x}_t - \beta_A^T a_t), \quad (3)$$

where  $\tau_0 = -\infty$  and  $\tau_C = \infty$ . To obtain the optimal thresholds, this ordinal regression model is fitted for  $N$  sequences with the following objective function

$$L(\theta, \beta_{\mathbf{X}}, \beta_A) = -\frac{1}{NT} \sum_{n=1}^N \sum_{t=1}^T \sum_{c=1}^C \mathbb{I}((y_t)^n = c) \log(\Pr(Y = c | \mathbf{X} = (\mathbf{x}_t)^n, A = (a_t)^n)), \quad (4)$$

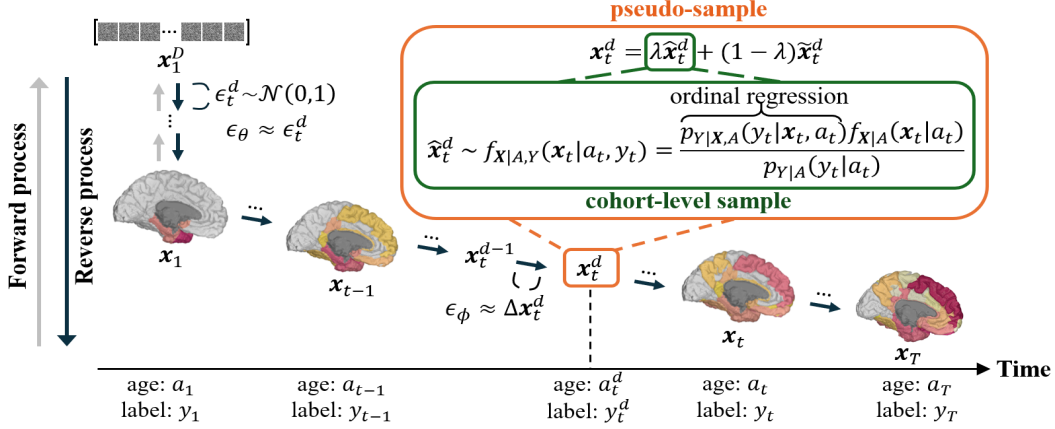


Figure 1: Overview of ConDOR. ConDOR generates longitudinal sequence  $\{\mathbf{x}_t\}_{t=1}^T$  conditioned on ordinal factors such as age  $\{a_t\}_{t=1}^T$  and progressive labels  $\{y_t\}_{t=1}^T$ . Baseline data  $\mathbf{x}_1$  is generated by Regional Diffusion Model  $\epsilon_\theta(\cdot)$  that estimates Gaussian noise  $\epsilon_t^d \sim N(0, 1)$ . To capture temporal changes within a sequence,  $\mathbf{x}_t^d$  is sampled for every  $d = 1, \dots, D$  diffusion step between two data points adjacent in time  $\{\mathbf{x}_{t-1}, \mathbf{x}_t\}$ . The  $\mathbf{x}_t^d$  is a combination of cohort-level and subject-level samples (i.e.,  $\hat{\mathbf{x}}_t^d$  and  $\tilde{\mathbf{x}}_t^d$ ) that considers general trend at the cohort-level and subject-specific progression for given conditions, respectively. Given the  $\mathbf{x}_t^d$ , Temporal Diffusion Model  $\epsilon_\phi(\cdot)$  learns the difference  $\Delta \mathbf{x}_t^d = \mathbf{x}_t^d - \mathbf{x}_{t-1}^d$  to generate follow-up data  $\{\mathbf{x}_t\}_{t=2}^T$ .

where  $\mathbb{I}(y_t = c)$  is an indicator function that outputs 1 if the label  $y_t$  is  $c$  and 0 otherwise. With this loss, thresholds are optimized to maximize the likelihood of accurately predicting ordinal samples.

**Modeling  $f_{\mathbf{X}|A}(\mathbf{x}_t|a_t)$  via kernel density estimation.** As the distribution of  $\mathbf{x}_t$  is unknown, we use a non-parametric KDE to estimate  $f_{\mathbf{X}|A}(\mathbf{x}_t|a_t)$  from the available data. Given ROI-wise measurements  $\mathbf{x}_t = [x_{t,1}, \dots, x_{t,B}] \in \mathbb{R}^B$ , the prior distribution  $f_{\mathbf{X}|A}(\mathbf{x}_t|a_t)$  is derived as

$$f_{\mathbf{X}|A}(\mathbf{x}_t|a_t) = \prod_{b=1}^B f_{X_b|A}(x_{t,b}|a_t) = \prod_{b=1}^B \frac{1}{N} \sum_{n=1}^N \sum_{t=1}^T \frac{1}{h_b} k\left(\frac{x_{t,b} - (x_{t,b})^n}{h_b}\right), \quad (5)$$

where  $h_b$  is a bandwidth of the Gaussian kernel  $k(\cdot)$ . By integrating this distribution with the  $p_{Y|\mathbf{X},A}(y_t|\mathbf{x}_t, a_t)$  from equation 3, the  $f_{\mathbf{X}|A,Y}(\mathbf{x}_t|a_t, y_t)$  is derived as in equation 1.

**Inverse transform sampling of  $\mathbf{x}$ .** After estimating the conditional PDF  $f_{\mathbf{X}|A,Y}(\mathbf{x}_t|a_t, y_t)$ , inverse transform sampling (Devroye, 1986) is performed to generate the brain measurements  $\mathbf{x}_t$  given its age and disease label. This is done by calculating its cumulative distribution function (CDF) as

$$F_{\mathbf{X}|A,Y}(\mathbf{x}_t|a_t, y_t) = \prod_{b=1}^B F_{X_b|A,Y}(x_{t,b}|a_t, y_t) = \prod_{b=1}^B \int_{-\infty}^{x_{t,b}} f_{X_b|A,Y}(u|a_t, y_t) du, \quad (6)$$

which denotes the probability that  $X_b$  take values less than or equal to  $x_{t,b}$  for given conditions  $a_t$  and  $y_t$ . Thus, given  $\mathbf{u} = [u_1, \dots, u_B] \sim \text{Uniform}(0, 1)^B$ , the inverse CDF  $F_{\mathbf{X}|A,Y}^{-1}(\mathbf{u}|a_t, y_t)$  finds the  $\mathbf{x}_t = [x_{t,1}, \dots, x_{t,B}]$  such that each element satisfies  $F_{X_b|A,Y}(x_{t,b}|a_t, y_t) = u_b$ .

### 2.3 CONDOR: CONDITIONAL DIFFUSION MODEL USING ORDINAL REGRESSION

Fig. 1 illustrates the overall architecture of ConDOR that generates longitudinal samples  $\{\mathbf{x}_t\}_{t=1}^T$  given a sequence of ages  $\{a_t\}_{t=1}^T$  and labels  $\{y_t\}_{t=1}^T$ . As the  $\{\mathbf{x}_t\}_{t=1}^T$  is an entangled representation of *both spatial and temporal features*, our method characterizes each feature by using two separate diffusion models: Regional Diffusion Model (RDM)  $\epsilon_\theta(\cdot)$  and Temporal Diffusion Model (TDM)  $\epsilon_\phi(\cdot)$ , parameterized by  $\theta$  and  $\phi$ , respectively. Specifically, ConDOR operates as an autoregressive model, where RDM generates the sample for baseline time point  $\mathbf{x}_1$ , and TDM sequentially generates subsequent samples  $\{\mathbf{x}_t\}_{t=2}^T$ . While RDM captures features from distinct regions within the data, TDM captures temporal features at both cohort-level and subject-level by combining two separate samples: one is derived from a whole cohort distribution and the other is estimated from an individual sequence. The details of each diffusion model are given below.

### 2.3.1 REGIONAL DIFFUSION MODEL FOR BASELINE DATA GENERATION

Since sample  $\mathbf{x}_1$  at baseline time point is inherently absent of temporal prior features, RDM generates the baseline data by only accounting for their spatial representations. Building upon the Denoising Diffusion Probabilistic Model (DDPM) (Ho et al., 2020), RDM is crafted as a conditional diffusion model that treats  $\mathbf{x}_t$  ( $t = 1, \dots, T$ ) as independent cross-sectional data. Its forward process  $q(\cdot)$  gradually adds Gaussian noise  $\epsilon_t^d \sim \mathcal{N}(0, 1)$  to  $\mathbf{x}_t$  for  $D$  diffusion steps as

$$q(\mathbf{x}_t^{1:D} | \mathbf{x}_t^0) := \prod_{d=1}^D q(\mathbf{x}_t^d | \mathbf{x}_t^{d-1}) := \prod_{d=1}^D \mathcal{N}(\mathbf{x}_t^d; \sqrt{1 - \beta_t^d} \mathbf{x}_t^{d-1}, \beta_t^d \mathbf{I}), \quad (7)$$

where  $\mathbf{x}_t^0 = \mathbf{x}_t$  and  $\beta_t^d$  is a variance schedule of the Gaussian distribution. During training, a reverse process  $p_\theta(\cdot)$  reconstructs samples conditioned on  $a_t$  and  $y_t$  by estimating the noise as follows:

$$p_\theta(\mathbf{x}_t^{0:D} | a_t, y_t) := p(\mathbf{x}_t^D) \prod_{d=1}^D \mathcal{N}(\mathbf{x}_t^{d-1}; \mu_\theta(\mathbf{x}_t^d, a_t, y_t, d), \beta_t^d \mathbf{I}), \quad (8)$$

where the mean of Gaussian distribution  $\mu_\theta(\mathbf{x}_t^d, a_t, y_t, d)$  is determined by a neural network  $\epsilon_\theta(\mathbf{x}_t^d, a_t, y_t, d)$  (i.e., conditional U-Net (Ronneberger et al., 2015)). To reconstruct samples from a complete Gaussian noise, RDM is trained to estimate the diffusion step-wise noise  $\epsilon_t^d$  with the following loss

$$L_{\text{RDM}} = \mathbb{E}_{\mathbf{x}_t, d, \epsilon_t^d \sim \mathcal{N}(0, 1)} \|\epsilon_t^d - \epsilon_\theta(\mathbf{x}_t^d, a_t, y_t, d)\|^2, \quad (9)$$

so that the baseline time point data are produced during the sampling process.

### 2.3.2 TEMPORAL DIFFUSION MODEL FOR FOLLOW-UP DATA GENERATION

To characterize temporal features within sequences, TDM is trained to learn changes among samples at different time points. As prior samples are highly likely to affect subsequent data, TDM operates as an autoregressive model that sequentially reconstructs the follow-up sample from the previous one, using the prior as a reference. Specifically, while RDM generates  $\mathbf{x}_1$  from Gaussian noise, TDM generates  $\mathbf{x}_t$  ( $t \geq 2$ ) based on the prior data  $\mathbf{x}_{t-1}$ . In other words, TDM treats the previous data like a complete noise  $\mathbf{x}_t^D$  in RDM, thereby eliminating the need for forward diffusion since the noise (i.e., baseline data) is already given. The reconstruction of follow-up data is done by a reverse diffusion for  $D$  steps between every data pair adjacent in time  $\{\mathbf{x}_{t-1}, \mathbf{x}_t\}_{t=2}^T$ , i.e., sampling pseudo-samples  $\{\mathbf{x}_t^d\}_{d=1}^D$  for each pair. Similar to RDM which estimates stepwise noises, TDM estimates the difference between  $\mathbf{x}_t^{d-1}$  and  $\mathbf{x}_t^d$ , enabling the model to learn temporal changes efficiently.

Given that the diffusion steps  $d = 1, \dots, D$  of TDM correspond to the subdivided time between the real time points  $t - 1$  and  $t$ , the diffusion step-wise age  $a_t^d$  and label  $y_t^d$  are defined as follows:

$$a_t^d = a_{t-1} + (a_t - a_{t-1}) \frac{d}{D} \quad \text{and} \quad y_t^d = \min \left\{ c \in \{1, \dots, C\} : c \geq y_{t-1} + (y_t - y_{t-1}) \frac{d}{D} \right\}, \quad (10)$$

The  $a_t^d$  represents an interpolated age between  $a_{t-1}$  and  $a_t$ , and the  $y_t^d$  indicates a discretized label for the intermediate diffusion step. For example, if  $y_{t-1}$  is 1 (e.g., healthy) and the following label  $y_t$  is  $C$  (e.g., the most deteriorated stage),  $y_t^d$  sequentially advances from 1 to  $C$  as the diffusion progresses. These interpolated conditions allow TDM to account for smooth transitions between different time points and incorporate temporal dynamics into the diffusion process.

**Integrating cohort-level sample & subject-level sample.** Given conditions  $a_t^d$  and  $y_t^d$ , the pseudo-sample  $\mathbf{x}_t^d$  at diffusion step  $d$  is derived as a linear combination of  $\hat{\mathbf{x}}_t^d$  and  $\tilde{\mathbf{x}}_t^d$  as follows:

$$\mathbf{x}_t^d = \lambda \hat{\mathbf{x}}_t^d + (1 - \lambda) \tilde{\mathbf{x}}_t^d, \quad (11)$$

where  $\hat{\mathbf{x}}_t^d \sim f_{\mathbf{X}|A,Y}(\mathbf{x}_t | a_t, y_t)$  is a *cohort-level* sample drawn from the overall cohort distribution defined in equation 1. This represents a sample that captures general trends of a population based on the given age and label. In contrast,  $\tilde{\mathbf{x}}_t^d = \mathbf{x}_{t-1} + (\mathbf{x}_t - \mathbf{x}_{t-1}) \frac{d}{D}$  is a *subject-level* sample, which is a set of interpolated brain measurements between two consecutive time points. This accounts for individual-specific changes in the brain over time. The  $\lambda \in [0, 1]$  is a hyperparameter that balances the trade-off between cohort and subject-level information. Higher  $\lambda$  emphasizes the global pattern at the cohort level, while lower  $\lambda$  focuses more on the subject-specific trajectory. This approach enables the model to integrate both population-wide and individual-specific features flexibly.

Given the integrated sample  $\mathbf{x}_t^d$ , TDM estimates the differences  $\Delta\mathbf{x}_t^d = \mathbf{x}_t^d - \mathbf{x}_t^{d-1}$  at each diffusion step  $d = 1, \dots, D$ , where  $\mathbf{x}_t^0 = \mathbf{x}_{t-1}$  and  $\mathbf{x}_t^D = \mathbf{x}_t$ . For  $t = 2, \dots, T$ , the model  $\epsilon_\phi(\cdot)$  approximates the difference  $\Delta\mathbf{x}_t^d$  with the following loss function

$$L_{\text{TDM}} = \mathbb{E}_{\mathbf{x}_t, d, \Delta\mathbf{x}_t^d} [\|\Delta\mathbf{x}_t^d - \epsilon_\phi(\{\mathbf{x}_t^d, a_t, y_t\}_{t-1}^t, d)\|^2], \quad (12)$$

so that follow-up samples  $\{\mathbf{x}_t\}_{t=2}^T$  are reconstructed by learning detailed changes within sequences.

## 2.4 MULTI-DOMAIN LEARNING WITH A DOMAIN CONDITION

Given that medical data analysis is inherently challenged by class imbalance and limited data availability due to costly data acquisition processes, integrating multi-source data is necessary to ensure robust and generalizable learning. Therefore, ConDOR provides an extended generative scheme by integrating longitudinal data from multiple domains while preserving domain-specific features. This is done by using an additional domain condition for reverse processes in Regional and Temporal Diffusion Models. Unlike time-varying age and label conditions, the domain does not depend on time, thereby an identical domain condition is consistently applied across all time points.

**Regional Diffusion Model with a domain condition.** Given  $K$  domains, let  $m_k$  ( $k = 1, \dots, K$ ) be a domain type. The reverse process of RDM with this additional domain condition is defined as

$$p_\theta(\mathbf{x}_t^{0:D} | a_t, y_t, m_k) := p(\mathbf{x}_t^D) \prod_{d=1}^D \mathcal{N}(\mathbf{x}_t^{d-1}; \mu_\theta(\mathbf{x}_t^d, a_t, y_t, m_k, d), \beta_t^d \mathbf{I}), \quad (13)$$

where the  $\mu_\theta$  is determined by a neural network  $\epsilon_\theta(\cdot)$  trained with the following denoising objective

$$L_{\text{RDM}} = \mathbb{E}_{\mathbf{x}_t, d, \epsilon_t^d \sim N(0,1)} \|\epsilon_t^d - \epsilon_\theta(\mathbf{x}_t^d, a_t, y_t, m_k, d)\|^2. \quad (14)$$

This allows RDM to estimate the noise  $\epsilon_t^d$  while incorporating the domain condition, so that RDM generates domain-specific data, enhancing the quality and relevance of the generated samples.

**Temporal Diffusion Model with a domain condition.** Let  $N_k$  be the number of sequences for domain  $m_k$ , and  $M$  be a random variable that denotes the domain condition. With the  $M$ , the equation 1 is rewritten as a mixture distribution  $\bar{f}_{\mathbf{X}|A,Y,M}(\cdot)$  as follows:

$$\bar{f}_{\mathbf{X}|A,Y,M}(\mathbf{x}_t | a_t, y_t, m_k) = \sum_{k=1}^K \alpha_k f_{\mathbf{X}|A,Y,M}^k(\mathbf{x}_t | a_t, y_t, m_k), \quad (15)$$

where  $\alpha_k = \frac{N_k}{\sum_{k=1}^K N_k}$  is a mixing coefficient for a domain-specific PDF  $f_{\mathbf{X}|A,Y,M}^k(\cdot)$ . This mixture density allows small sample-sized domains (or domains with class imbalances) to be enriched by incorporating other larger domains (or domains with more balanced classes), thereby mitigating the risk of overfitting to limited data. From the mixture density, a cohort-level sample  $\hat{\mathbf{x}}_t^d \sim \bar{f}_{\mathbf{X}|A,Y,M}(\mathbf{x}_t | a_t, y_t, m_k)$  is obtained to further construct the  $\mathbf{x}_t^d$  as in equation 11. Along with the age and label conditions, the domain condition  $m_k$  is inputted into TDM  $\epsilon_\phi(\cdot)$  to estimate the diffusion step-wise difference  $\Delta\mathbf{x}_t^d = \mathbf{x}_t^d - \mathbf{x}_t^{d-1}$  by using the following loss function

$$L_{\text{TDM}} = \mathbb{E}_{\mathbf{x}_t, d, \Delta\mathbf{x}_t^d} \|\Delta\mathbf{x}_t^d - \epsilon_\phi(\{\mathbf{x}_t^d, a_t, y_t\}_{t-1}^t, m_k, d)\|^2. \quad (16)$$

With this loss, the generated samples accurately reflect the underlying characteristics of each domain while still accounting for the ordinal nature of the age and label conditions.

## 3 RELATED WORKS

**Longitudinal Data Analysis.** In contrast to cross-sectional studies that focus on a snapshot of data at a single point in time, longitudinal data analyses focus on understanding temporal dynamics within data over time. This approach is widely used in modeling time-series data in various domains such as healthcare (Mosquera et al., 2023; Yoon et al., 2023; Hwang et al., 2019), traffic flow forecasting (Shu et al., 2021; Li & Zhu, 2021), and computer vision tasks such as human motion recognition in videos (Chen et al., 2021; Cheng et al., 2020). In particular, studies in the healthcare domain include tracking electronic health records (Joshua Lin et al., 2022), predicting adolescent brain development (Holm et al., 2023), and modeling the progression of diseases (Hwang et al.,

2019). By tracking health outcomes over time, these long-term studies contribute to the understanding of the progression of disorders and provide critical insights into how patient outcomes evolve.

**Generative Models for Tabular Data.** Tabular data are ubiquitous in various fields such as medicine, economics, and marketing, often involving a mix of discrete and continuous variables. Recent generative methods handle both types simultaneously (Xu et al., 2019; Zhao et al., 2021; Kotelnikov et al., 2023), rather than focusing on either type (Choi et al., 2017). While these methods have shown successful results on tabular data, many are limited to cross-sectional data, failing to capture temporal dynamics in longitudinal data. This shortfall is particularly critical in healthcare, where understanding the evolution of patient health is essential for precise prognosis and treatment planning. To address the challenge, our method focuses on generating realistic longitudinal tabular data (i.e., biomarkers) that not only considers the intricate relationships between heterogeneous variables but also accurately characterizes temporal features across different time points.

## 4 EXPERIMENT

In this section, we describe the quantitative comparison of ConDOR with nine baseline methods and discuss the effect of model components along with interpretations. Overall, we performed experiments on four different biomarkers from MRI and PET images provided by two independent longitudinal Alzheimer’s disease (AD) studies: Alzheimer’s Disease Neuroimaging Initiative (ADNI) and Open Access Series of Imaging Studies (OASIS), whose demographics and preprocessing methods are reported in Appendix A. Also, we provide detailed implementation settings of ConDOR in Appendix B and extensive qualitative comparisons with the baseline models in Appendix D.

### 4.1 DATASETS

**ADNI.** ADNI study (Mueller et al., 2005) is the largest long-term study of AD, aimed at collecting a comprehensive set of biomarker data from participants over an extended period. Four AD-associated biomarkers (Ortner et al., 2019) collected from MRI and PET scans were used: (1) Cortical Thickness (CT) from MRI, Standardized Uptake Value Ratio (SUVR) of (2) Amyloid, (3) fluorodeoxyglucose (FDG), and (4) Tau from PET. From  $N=2153$  subjects, we excluded those with a single time point, resulting in 178, 687, 678, and 166 subjects for CT, Amyloid, FDG, and Tau respectively, with time points  $T$  per participant ranging from 2 to 10. All biomarkers were measured from 148 ROIs parcellated based on the Destrieux atlas (Destrieux et al., 2010). Five diagnostic labels were used: Cognitively Normal (CN), Significant Memory Concern (SMC), Early Mild Cognitive Impairment (EMCI), Late MCI (LMCI), and AD, with the disease progressing irreversibly from CN to AD.

**OASIS.** Compared to the ADNI, OASIS dataset (LaMontagne et al., 2019) provides a relatively small data where only Tau is available for  $N=32$  subjects. All subjects have two time points, spaced 6 months apart, each labeled CN or AD. Among the 32 subjects, three were diagnosed with AD, where only one of them was consistently diagnosed with AD at both time points, while the other two transitioned from CN to AD. As in the ADNI, Tau was measured at 148 ROIs based on the Destrieux atlas. Due to the small sample size with a biased label distribution, single-domain learning on the OASIS dataset is highly prone to overfitting. Thus, we performed multi-domain learning on the Tau of ADNI and OASIS together with a domain condition to improve the model’s generalizability.

### 4.2 EXPERIMENTAL SETUP

**Baseline methods.** We utilized nine baseline models, encompassing various types of generative models such as normalizing flow, generative adversarial networks (GANs), variational autoencoders (VAEs), diffusion models, and traditional interpolation-based synthetic techniques. Specifically, SMOTE (Chawla et al., 2002) is an interpolation-based method that synthesizes data points as a convex combination of a real data point with its  $k$ -th nearest neighbor. This is a simple yet effective solution as demonstrated in (Camino et al., 2020; Kotelnikov et al., 2023), where it outperforms GANs and diffusion models for tabular data generation. Also, we adopt Conditional Recurrent Flow (CRoW) (Hwang et al., 2019), a conditional normalizing flow model that generates long-term sequences. We also included GANs such as Conditional Tabular GAN (CTGAN) (Xu et al., 2019), Conditional Table GAN (CTAB-GAN) (Zhao et al., 2021), and CTAB-GAN+ (Zhao et al., 2024). For VAEs, we adopt Generative Modelling with Graph Learning (GOGGLE) (Liu et al., 2023) and TVAE, which is VAE (Kingma, 2013) for tabular data generation introduced in (Xu et al., 2019). Lastly, diffusion-based models such as TabDDPM (Kotelnikov et al., 2023) and a conditional form of Denoising Diffusion Probabilistic Model (DDPM) (Ho et al., 2020) are adopted.

Table 1: Generation performance for single-domain learning on CT, Amyloid, and FDG test sets, with averages and standard deviations from three replicates. The best results are in bold, and the second-best are underlined.

Model	Cortical Thickness			Amyloid			FDG		
	WD	RMSE	JSD	WD	RMSE	JSD	WD	RMSE	JSD
SMOTE	8.68 ± 0.0	0.57 ± 0.0	0.025 ± 0.0	5.82 ± 0.0	0.34 ± 0.0	0.014 ± 0.0	3.19 ± 0.0	0.10 ± 0.0	0.002 ± 0.0
CRow	<u>5.13 ± 0.13</u>	0.78 ± 0.014	0.042 ± 0.001	<u>5.37 ± 0.40</u>	0.85 ± 0.023	0.061 ± 0.011	<u>2.86 ± 0.04</u>	0.37 ± 0.007	0.012 ± 0.0
CTGAN	7.90 ± 0.12	0.37 ± 0.005	0.022 ± 0.001	11.00 ± 0.02	0.43 ± 0.001	0.036 ± 0.0	4.52 ± 0.02	0.13 ± 0.001	0.003 ± 0.0
CTAB-GAN	6.43 ± 0.29	0.35 ± 0.033	0.016 ± 0.001	7.93 ± 0.63	0.42 ± 0.034	0.023 ± 0.004	3.47 ± 0.03	0.11 ± 0.002	<u>0.002 ± 0.0</u>
CTAB-GAN+	6.09 ± 0.40	<u>0.34 ± 0.054</u>	0.014 ± 0.001	6.50 ± 0.29	0.35 ± 0.017	0.015 ± 0.001	3.58 ± 0.03	0.11 ± 0.007	<u>0.002 ± 0.0</u>
GOGGLE	8.05 ± 0.39	<u>0.34 ± 0.016</u>	0.020 ± 0.001	16.62 ± 0.16	0.65 ± 0.006	0.010 ± 0.0	9.33 ± 0.22	0.25 ± 0.006	0.010 ± 0.002
TVAE	5.69 ± 0.59	0.38 ± 0.053	<u>0.013 ± 0.003</u>	7.24 ± 0.21	0.39 ± 0.030	0.015 ± 0.002	4.52 ± 0.42	0.16 ± 0.019	0.004 ± 0.001
DDPM	9.71 ± 3.94	0.59 ± 0.160	0.028 ± 0.017	9.34 ± 2.51	0.66 ± 0.282	0.026 ± 0.015	2.90 ± 0.46	0.10 ± 0.015	<b>0.001 ± 0.001</b>
TabDDPM	14.23 ± 0.02	0.61 ± 0.0	0.070 ± 0.001	31.28 ± 0.05	1.18 ± 0.001	0.145 ± 0.001	11.59 ± 0.04	0.32 ± 0.001	0.018 ± 0.0
ConDOR	<b>4.25 ± 0.02</b>	<b>0.21 ± 0.002</b>	<b>0.007 ± 0.001</b>	<b>5.27 ± 0.09</b>	<b>0.31 ± 0.012</b>	<b>0.008 ± 0.001</b>	<b>2.49 ± 0.02</b>	<b>0.09 ± 0.001</b>	<b>0.001 ± 0.0</b>

Table 2: Generation performance for multi-domain learning on Tau of ADNI and OASIS test sets. The average of three replicates and their standard deviations are reported along with the generation time for sampling 36 sequences (i.e., the number of test data) and the average time per sequence.

Model	WD	RMSE	JSD	Test set gen. time (s)	Per-seq. gen. time (s)
SMOTE	7.146 ± 0.0	0.460 ± 0.0	0.029 ± 0.0	29.85	0.83
CRow	9.494 ± 0.188	0.599 ± 0.027	0.045 ± 0.045	<b>1.39</b>	<b>0.04</b>
CTGAN	19.545 ± 0.416	0.441 ± 0.014	0.280 ± 0.025	2.97	0.08
CTAB-GAN	8.950 ± 0.512	0.455 ± 0.036	0.078 ± 0.011	26.60	0.74
CTAB-GAN+	7.738 ± 1.211	0.393 ± 0.048	0.034 ± 0.005	48.90	1.36
GOGGLE	8.380 ± 0.445	0.343 ± 0.014	<b>0.012 ± 0.0</b>	2.08	0.06
TVAE	<b>5.096 ± 0.303</b>	0.300 ± 0.020	<u>0.018 ± 0.003</u>	4.33	0.12
DDPM	9.671 ± 1.738	0.649 ± 0.235	0.032 ± 0.014	81.12	2.25
TabDDPM	50.592 ± 0.404	1.890 ± 0.018	0.400 ± 0.0	151.09	4.20
ConDOR (Ours)	5.625 ± 0.040	<b>0.293 ± 0.011</b>	<b>0.012 ± 0.0</b>	65.7	1.83

**Evaluation.** Following a prior work (Kotelnikov et al., 2023), three metrics were used to evaluate the difference between generated samples and the test data: (1) Wasserstein distance (**WD**), (2) Root mean squared error (**RMSE**), and (3) **Jensen-Shannon divergence (JSD)**. WD measures the expected minimum distance to transform one distribution into another, primarily reflecting differences in the global structure of the two distributions. In contrast, RMSE emphasizes detailed sample-wise differences, as it calculates the squared error for each pair of points. Similarly, JSD is sensitive to imbalances between distributions, capturing the differences in distributional shape and entropy. For all experiments, we used 80% of the whole data for training and the rest 20% for testing. The number of sampled data is equal to the number of test data in each respective experiment. All baselines and our model were trained three times to report their average results with standard deviation.

### 4.3 QUANTITATIVE RESULTS

**Single-domain learning.** Table 1 presents the quantitative results from the single-domain experiments on CT, Amyloid, and FDG. In all experiments and across all metrics, ConDOR consistently outperformed all baseline methods. Specifically, in the CT experiment, ConDOR demonstrated far smaller RMSE by a margin of 0.57 over CRow and at least 0.13 over GOGGLE and CTAB-GAN+. In the Amyloid experiment, ConDOR achieved up to 26.01 lower WD than TabDDPM and at least 0.1 lower than CRow. Although the margin over CRow is small on WD, our method significantly outperformed CRow on RMSE and JSD by margins of 0.54 and 0.053, respectively. Note that RMSE and JSD are sensitive to sample-wise differences and distributional imbalances, while WD mainly focuses on global structural differences, such as mean differences between distributions. Thus, these results suggest that ConDOR is more effective in *capturing individual characteristics with high variance* compared to CRow. In the FDG experiment, ConDOR surpassed all baselines in WD and RMSE, and both our method and DDPM achieved the best result on JSD.

**Multi-domain learning.** As the sample size of the OASIS is small and label distribution is biased, the Tau of ADNI and OASIS were merged into a unified dataset and learned together using a domain condition. Table 2 shows quantitative results from the unified dataset and sampling times. ConDOR surpassed eight out of nine baselines across all distance metrics and achieved comparable results to GOGGLE and TVAE. Specifically, our method and GOGGLE showed the same 0.012 on JSD, and TVAE surpassed our method on WD by  $\sim 0.55$ . However, ConDOR far outperformed GOGGLE on WD and RMSE by  $\sim 2.7$  and 0.05, respectively, and exceeded TVAE on RMSE and JSD. These results suggest that although TVAE better estimates the overall distribution shape, our method excels in preserving finer details by capturing outliers and subtle differences at specific data points.

To assess computational efficiency, we measured the time taken to generate 36 sequences, corresponding to the test data size. As a result, CRow was the fastest taking  $\sim 1.4$  seconds, and our



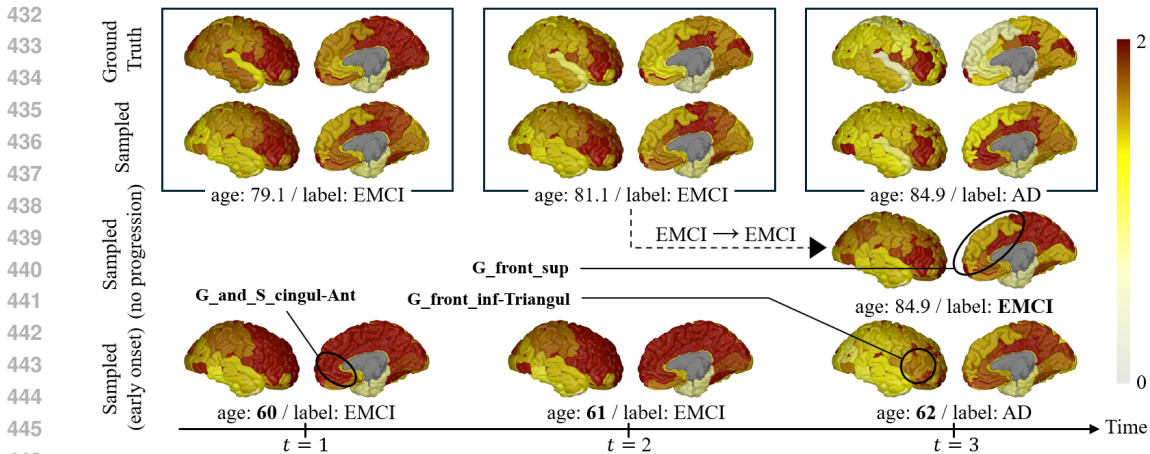


Figure 2: Visualization of generation results from the FDG experiment (subject ID: 130\_S\_2403). The first row shows the ground truth sequence with three time points and the second panel shows the generated sequence from ConDOR for the same temporal conditions which highly resemble the real samples. In the third row, brain measurements are generated assuming the disease has not manifested at  $t = 3$ , while the bottom shows the sampled results with the same label condition as the ground truth with younger ages in sixties.

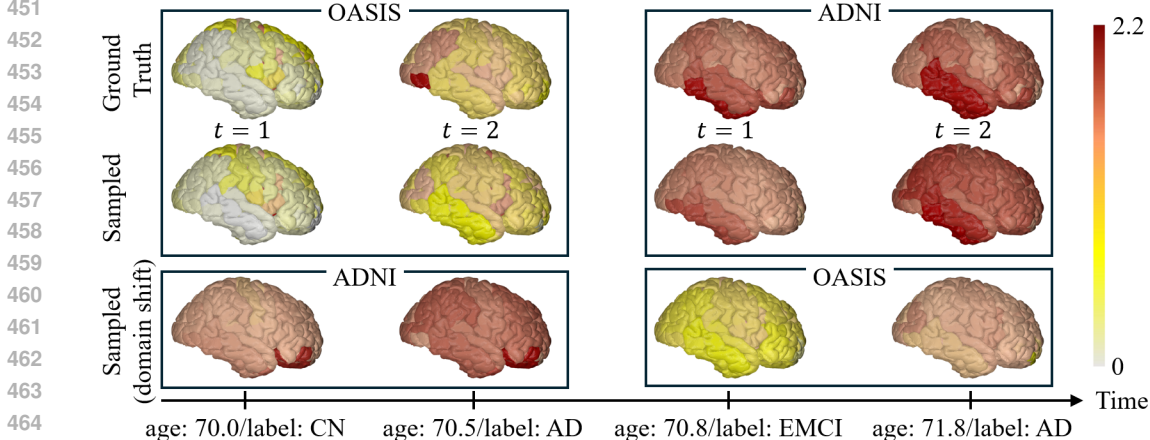


Figure 3: Visualization of generated results from the Tau experiment and results with switched domain conditions. The top panel is the ground truth of two samples with two time points (subject ID: OAS30818 and 129\_S\_4422 for OASIS and ADNI, respectively), where the data from different domains show different characteristics. The second panel shows generated results from ConDOR, and the bottom panel shows results with reversed domain conditions while age and label are consistent.

method took  $\sim 66$  seconds. In general, this increased sampling time was typical for diffusion-based methods such as DDPM, TabDDPM, and ConDOR, due to the iterative denoising steps in the sampling process. However, as shown in both Table 1 and Table 2, the sample quality of our method far surpasses other models, showing a trade-off between quality and computation speed.

#### 4.4 MODEL BEHAVIOR AND ABLATION STUDY

**Analyses on conditions.** Figures 2 and 3 illustrate qualitative results from ConDOR on the FDG and Tau experiments, respectively, highlighting the impact of label, age, and domain conditions. Given that FDG SUVR generally decreases with AD progression (Mosconi et al., 2009) while Tau SUVR increases (Sjögren et al., 2001), these trends are accurately reflected in the generated results. For example, the top row in Fig. 2 is the ground truth and the second row is the generated sequence from ConDOR with the same conditions, where regional results resemble the ground truth for all time points. The third row illustrates a label-consistent scenario, where the disease has not progressed from EMCI to AD. In this case, the FDG SUVR at  $t = 3$  remains higher than that of AD in the second panel, which demonstrates the sensitivity of ConDOR that captures subtle differences between labels. One of the most prominent differences is shown in the *superior frontal gyrus*, where significant glucose reduction has been observed along the AD progression in various AD studies (Sanabria-Diaz et al., 2013; He et al., 2015). While both the ground truth and generated

Table 3: Ablation studies on the cohort-level sample weight  $\lambda$  for all experiments.

$\lambda$	ADNI						ADNI+OASIS	
	Cortical Thickness		Amyloid		FDG		Tau	
	WD	RMSE	WD	RMSE	WD	RMSE	WD	RMSE
0	4.423 $\pm$ 0.115	0.208 $\pm$ 0.003	5.608 $\pm$ 0.070	0.321 $\pm$ 0.010	2.551 $\pm$ 0.072	0.086 $\pm$ 0.002	6.628 $\pm$ 0.286	0.334 $\pm$ 0.016
0.1	<b>4.252 <math>\pm</math> 0.024</b>	<b>0.205 <math>\pm</math> 0.002</b>	<b>5.400 <math>\pm</math> 0.139</b>	0.313 $\pm$ 0.012	<b>2.487 <math>\pm</math> 0.015</b>	<b>0.085 <math>\pm</math> 0.001</b>	6.172 $\pm$ 0.188	0.320 $\pm$ 0.007
0.3	4.368 $\pm$ 0.135	0.208 $\pm$ 0.007	5.522 $\pm$ 0.173	<b>0.296 <math>\pm</math> 0.012</b>	2.512 $\pm$ 0.002	0.086 $\pm$ 0.002	5.833 $\pm$ 0.163	0.313 $\pm$ 0.007
0.5	4.372 $\pm$ 0.064	0.207 $\pm$ 0.004	5.541 $\pm$ 0.088	0.326 $\pm$ 0.088	2.595 $\pm$ 0.031	0.088 $\pm$ 0.001	5.692 $\pm$ 0.069	0.305 $\pm$ 0.008
0.7	4.496 $\pm$ 0.035	0.215 $\pm$ 0.002	5.530 $\pm$ 0.086	0.318 $\pm$ 0.012	2.567 $\pm$ 0.024	0.087 $\pm$ 0.001	<b>5.645 <math>\pm</math> 0.024</b>	<b>0.292 <math>\pm</math> 0.010</b>
0.9	4.372 $\pm$ 0.083	0.217 $\pm$ 0.012	5.629 $\pm$ 0.029	<b>0.309 <math>\pm</math> 0.007</b>	2.632 $\pm$ 0.108	0.088 $\pm$ 0.002	5.999 $\pm$ 0.223	0.313 $\pm$ 0.003
1	4.432 $\pm$ 0.122	0.209 $\pm$ 0.005	5.852 $\pm$ 0.287	0.331 $\pm$ 0.008	2.620 $\pm$ 0.046	0.088 $\pm$ 0.002	5.832 $\pm$ 0.207	0.313 $\pm$ 0.023

results with the AD label show relatively low FDG SUVR in this area, the sampled EMCI results at the same age display higher values, resembling the ground truth of the EMCI.

On the other hand, in the early-onset AD (EOAD) scenario (i.e., AD diagnosed before the age of 65) on the bottom row, ROIs such as *the cingulate gyrus and sulcus* show higher FDG SUVR than the ground truth, which is known to be a highly negatively correlated region with age (Jiang et al., 2018). Also, it is worth noting that *the triangular part of the inferior frontal gyrus* of the EOAD shows lower values than late-onset AD (LOAD). This result aligns with established AD studies (Kim et al., 2005; Kalpouzos et al., 2005), which have shown that EOAD features more focal reductions in glucose metabolism in *the frontal cortex*, while LOAD tends to have more diffuse hypometabolism.

Fig. 3 illustrates results from the Tau experiment involving two samples each from the OASIS and ADNI datasets. Both samples span two time points with similar ages, yet the OASIS sample shifts from CN to AD, while the ADNI sample progresses from EMCI to AD. In the top row, the ground truth for AD of OASIS (2nd column) and AD of ADNI (4th column) show significant differences, despite similar ages, possibly due to differences in the data collection environment.

As shown in the second row, our method successfully captured these domain-specific differences. Moreover, when domain conditions are reversed (3rd row), ConDOR not only characterizes the distinct features of each domain but also accurately captures the positive correlation between Tau SUVR and disease progression. Specifically, the bottom left sample with the ADNI and CN conditions displays lower Tau SUVR than the ground truth of the ADNI EMCI (top, 3rd column). Similarly, the EMCI sample of OASIS (bottom, 3rd column) shows intermediate values between the CN and AD of OASIS. Given that the original OASIS dataset has only CN and AD labels, multi-domain learning with other sources, such as ADNI—which includes intermediate MCI labels—allows us to generate a broader spectrum of data. Such an approach empowers the model to learn the comprehensive, full progression from CN to AD, thereby enhancing its generalizability across different disease stages.

**Effect of the cohort-level weight  $\lambda$ .** Table 3 presents the result of the ablation study on the  $\lambda$ , which balances the effect of cohort-level and subject-level samples used in TDM. For all experiments, using both samples (i.e.,  $0 < \lambda < 1$ ) outperformed the settings using only subject-level (i.e.,  $\lambda = 0$ ) or cohort-level samples (i.e.,  $\lambda = 1$ ) alone. In the single-domain experiments on CT, Amyloid, and FDG,  $\lambda = 0.1$  yielded the best results. On the other hand, in the multi-domain experiment with Tau, higher  $\lambda$ 's such as  $\lambda = 0.7$  and  $0.5$  produced the best and second-best results, respectively. These findings suggest that using both cohort-level and individual-specific features improves the sample quality regardless of the domain settings. However, subject-specific details play a relatively critical role in single-domain learning, while capturing broader population-wide trends across multiple domains is more important when learning from diverse sources for effective generalization. Thus, by adjusting the  $\lambda$ , the model can generate higher-quality samples across both homogeneous and heterogeneous data, with the choice of  $\lambda$  varying based on the task and data distribution.

## 5 CONCLUSION

In this paper, we introduced ConDOR, a novel conditional diffusion model for generating longitudinal samples conditioned on multiple ordinal factors. When applied to the generation of costly longitudinal neurodegenerative disease data, ConDOR addresses the data scarcity issue in medical data analyses. By incorporating an ordinal regression model into the diffusion process, ConDOR effectively characterizes the realistic ordinal dynamics of the disease. Also, the model generates smooth temporal samples by employing a dual-sampling strategy, which blends both individual-specific and global characteristics obtained from the entire sample distribution. As a result, ConDOR outperformed nine recent generative methods, underscoring its potential to enhance our understanding of the complex relationships between heterogeneous disease-related factors and disease progression.

540 **Reproducibility Statement.** To ensure the reproducibility of our work, we provide a detailed dataset  
 541 description in Appendix A, and implementation settings including all hyperparameters in Appendix  
 542 B. Regarding quantitative evaluations, all experiments were replicated three times and their mean  
 543 with standard deviation is reported. We will release codes of our method and baseline methods along  
 544 with their pre-trained models publicly.

## 546 REFERENCES

- 547 Thomas Bayes. An essay towards solving a problem in the doctrine of chances. *Philosophical*  
 548 *transactions of the Royal Society of London*, (53):370–418, 1763.
- 549 Fabiola Becerra-Riera et al. On combining face local appearance and geometrical features for race  
 550 classification. In *Progress in Pattern Recognition, Image Analysis, Computer Vision, and Appli-*  
 551 *cations*, pp. 567–574. Springer, 2019.
- 552 Rebecca C Brown et al. Neurodegenerative diseases: an overview of environmental risk factors.  
 553 *Environmental health perspectives*, 113(9):1250–1256, 2005.
- 554 Ramiro D Camino et al. Oversampling tabular data with deep generative models: Is it worth the  
 555 effort? In *Advances in Neural Information Processing System (NeurIPS): "I Can't Believe It's*  
 556 *Not Better!" Workshop*, 2020.
- 557 Nitesh V Chawla et al. SMOTE: synthetic minority over-sampling technique. *Journal of artificial*  
 558 *intelligence research*, 16:321–357, 2002.
- 559 Yuxin Chen et al. Channel-wise topology refinement graph convolution for skeleton-based action  
 560 recognition. In *IEEE/CVF International Conference on Computer Vision (ICCV)*, pp. 13359–  
 561 13368, 2021.
- 562 Ke Cheng et al. Skeleton-based action recognition with shift graph convolutional network. In  
 563 *IEEE/CVF Conference on Computer Vision and Pattern Recognition (CVPR)*, pp. 183–192, 2020.
- 564 Edward Choi et al. Generating multi-label discrete patient records using generative adversarial  
 565 networks. In *Machine Learning for Healthcare Conference (MLHC)*, pp. 286–305. PMLR, 2017.
- 566 Scott E Counts et al. Biomarkers for the early detection and progression of Alzheimer’s disease.  
 567 *Neurotherapeutics*, 14(1):35–53, 2017.
- 568 Christophe Destrieux et al. Automatic parcellation of human cortical gyri and sulci using standard  
 569 anatomical nomenclature. *Neuroimage*, 53(1):1–15, 2010.
- 570 Luc Devroye. Sample-based non-uniform random variate generation. In *Winter Simulation Confer-*  
 571 *ence (WSC)*, pp. 260–265, 1986.
- 572 Oskar Hansson, Kaj Blennow, Henrik Zetterberg, and Jeffrey Dage. Blood biomarkers for  
 573 alzheimer’s disease in clinical practice and trials. *Nature aging*, 3(5):506–519, 2023.
- 574 Wei He et al. Meta-analytic comparison between PIB-PET and FDG-PET results in Alzheimer’s  
 575 disease and MCI. *Cell Biochemistry and Biophysics*, 71:17–26, 2015.
- 576 Jonathan Ho et al. Denoising diffusion probabilistic models. *Advances in Neural Information Pro-*  
 577 *cessing Systems (NeurIPS)*, 33:6840–6851, 2020.
- 578 Madelene C Holm et al. Linking brain maturation and puberty during early adolescence using  
 579 longitudinal brain age prediction in the ABCD cohort. *Developmental Cognitive Neuroscience*,  
 580 60:101220, 2023.
- 581 Makoto Hosono et al. Cumulative radiation doses from recurrent PET–CT examinations. *The British*  
 582 *Journal of Radiology*, 94(1126):20210388, 2021.
- 583 Seong Jae Hwang et al. Conditional recurrent flow: conditional generation of longitudinal samples  
 584 with applications to neuroimaging. In *IEEE/CVF International Conference on Computer Vision*  
 585 *(ICCV)*, pp. 10692–10701, 2019.

- 594 Clifford R Jack and David M Holtzman. Biomarker modeling of alzheimer’s disease. *Neuron*, 80  
595 (6):1347–1358, 2013.  
596
- 597 Jiehui Jiang et al. Study of the influence of age in 18F-FDG PET images using a data-driven ap-  
598 proach and its evaluation in Alzheimer’s disease. *Contrast media & molecular imaging*, 2018(1):  
599 3786083, 2018.
- 600 Sterling C Johnson et al. The Wisconsin registry for Alzheimer’s prevention: a review of findings  
601 and current directions. *Alzheimer’s & Dementia: Diagnosis, Assessment & Disease Monitoring*,  
602 10:130–142, 2018.  
603
- 604 Kueiyu Joshua Lin et al. Longitudinal data discontinuity in electronic health records and conse-  
605 quences for medication effectiveness studies. *Clinical Pharmacology & Therapeutics*, 111(1):  
606 243–251, 2022.
- 607 Grégoria Kalpouzou et al. Working memory and FDG–PET dissociate early and late onset Alzheimer  
608 disease patients. *Journal of Neurology*, 252(5):548–558, 2005.  
609
- 610 EJ Kim et al. Glucose metabolism in early onset versus late onset Alzheimer’s disease: an SPM  
611 analysis of 120 patients. *Brain*, 128(8):1790–1801, 2005.  
612
- 613 Diederik P Kingma. Auto-encoding variational bayes. *arXiv preprint arXiv:1312.6114*, 2013.
- 614 Akim Kotelnikov et al. TabDDPM: Modelling tabular data with diffusion models. In *International  
615 Conference on Machine Learning (ICML)*, pp. 17564–17579. PMLR, 2023.  
616
- 617 Zhanghui Kuang et al. Fashion retrieval via graph reasoning networks on a similarity pyramid. In  
618 *IEEE/CVF International Conference on Computer Vision (ICCV)*, pp. 3066–3075, 2019.
- 619 Pamela J LaMontagne et al. OASIS-3: longitudinal neuroimaging, clinical, and cognitive dataset  
620 for normal aging and Alzheimer disease. *medrxiv*, pp. 2019–12, 2019.  
621
- 622 Mengzhang Li and Zhanxing Zhu. Spatial-temporal fusion graph neural networks for traffic flow  
623 forecasting. In *AAAI conference on artificial intelligence (AAAI)*, volume 35, pp. 4189–4196,  
624 2021.
- 625 Tennison Liu et al. GOGGLE: Generative modelling for tabular data by learning relational structure.  
626 In *International Conference on Learning Representations (ICLR)*, 2023.  
627
- 628 Sheng Luo et al. Bayesian multiple imputation for missing multivariate longitudinal data from a  
629 Parkinson’s disease clinical trial. *Statistical methods in medical research*, 25(2):821–837, 2016.
- 630 Razvan V Marinescu et al. TADPOLE challenge: prediction of longitudinal evolution in Alzheimer’s  
631 disease. *arXiv preprint*, 2018.  
632
- 633 Lisa Mosconi et al. FDG-PET changes in brain glucose metabolism from normal cognition to patho-  
634 logically verified Alzheimer’s disease. *European Journal of Nuclear Medicine and Molecular  
635 Imaging*, 36:811–822, 2009.  
636
- 637 Lucy Mosquera et al. A method for generating synthetic longitudinal health data. *BMC Medical  
638 Research Methodology*, 23(1):67, 2023.
- 639 Susanne G Mueller et al. The Alzheimer’s disease neuroimaging initiative. *Neuroimaging Clinics  
640 of North America*, 15(4):869, 2005.  
641
- 642 Marion Ortner et al. Amyloid PET, FDG-PET or MRI?-the power of different imaging biomarkers  
643 to detect progression of early Alzheimer’s disease. *BMC neurology*, 19:1–6, 2019.
- 644 Emanuel Parzen. On estimation of a probability density function and mode. *The Annals of Mathe-  
645 matical Statistics*, 33(3):1065–1076, 1962.  
646
- 647 Jane S Paulsen et al. A review of quality of life after predictive testing for and earlier identification  
of neurodegenerative diseases. *Progress in neurobiology*, 110:2–28, 2013.

- 648 Olivier Querbes, Florent Aubry, Jérémie Pariente, Jean-Albert Lotterrie, Jean-François Démonet,  
649 Véronique Duret, Michele Puel, Isabelle Berry, Jean-Claude Fort, Pierre Celsis, et al. Early  
650 diagnosis of alzheimer’s disease using cortical thickness: impact of cognitive reserve. *Brain*, 132  
651 (8):2036–2047, 2009.
- 652 Olaf Ronneberger et al. U-Net: Convolutional networks for biomedical image segmentation. In *Med-*  
653 *ical Image Computing and Computer-Assisted Intervention (MICCAI)*, pp. 234–241. Springer,  
654 2015.
- 655 Gretel Sanabria-Diaz et al. Glucose metabolism during resting state reveals abnormal brain networks  
656 organization in the Alzheimer’s disease and mild cognitive impairment. *PloS one*, 8(7):e68860,  
657 2013.
- 658 Philine Schneider, Harald Hampel, and Katharina Buerger. Biological marker candidates of  
659 alzheimer’s disease in blood, plasma, and serum. *CNS neuroscience & therapeutics*, 15(4):358–  
660 374, 2009.
- 661 Wanneng Shu et al. A short-term traffic flow prediction model based on an improved gate recurrent  
662 unit neural network. *IEEE Transactions on Intelligent Transportation Systems*, 23(9):16654–  
663 16665, 2021.
- 664 Magnus Sjögren et al. Both total and phosphorylated tau are increased in Alzheimer’s disease.  
665 *Journal of Neurology, Neurosurgery & Psychiatry*, 70(5):624–630, 2001.
- 666 Chris Winship and Robert Mare. Regression models with ordinal variables. *American Sociological*  
667 *Review*, 49:512, 08 1984. doi: 10.2307/2095465.
- 668 Lei Xu et al. Modeling tabular data using conditional GAN. *Advances in Neural Information*  
669 *Processing Systems (NeurIPS)*, 32, 2019.
- 670 Minghao Xu et al. Self-supervised graph-level representation learning with local and global struc-  
671 ture. In *International Conference on Machine Learning (ICML)*, pp. 11548–11558. PMLR, 2021.
- 672 Chenggang Yan et al. Age-invariant face recognition by multi-feature fusion and decomposition with  
673 self-attention. *ACM Transactions on Multimedia Computing, Communications, and Applications*  
674 *(TOMM)*, 18(1s):1–18, 2022.
- 675 Fan Yang et al. Disentangled sequential graph autoencoder for preclinical Alzheimer’s disease char-  
676 acterizations from ADNI study. In *Medical Image Computing and Computer Assisted Intervention*  
677 *(MICCAI)*, pp. 362–372. Springer, 2021.
- 678 Jee Seok Yoon et al. SADM: Sequence-aware diffusion model for longitudinal medical image gen-  
679 eration. In *International Conference on Information Processing in Medical Imaging (IPMI)*, pp.  
680 388–400. Springer, 2023.
- 681 Zilong Zhao et al. CTAB-GAN: Effective table data synthesizing. In *Asian Conference on Machine*  
682 *Learning (ACML)*, pp. 97–112. PMLR, 2021.
- 683 Zilong Zhao et al. CTAB-GAN+: Enhancing tabular data synthesis. *Frontiers in Big Data*, 6:  
684 1296508, 2024.
- 685  
686  
687  
688  
689  
690  
691  
692  
693  
694  
695  
696  
697  
698  
699  
700  
701

In the appendix and supplementary material, we present **1)** the demographics of four biomarkers provided by ADNI and OASIS studies, **2)** detailed implementation settings of ConDOR used for each experiment, **3)** limitations of ConDOR and suggestions for future work, **4)** extensive qualitative comparisons with baseline methods, and **5)** a video illustrating a sampled sequence that shows changes in Amyloid SUVR over 20 years, which were not included in the main manuscript due to the page limit.

## A DATASET DEMOGRAPHICS

ADNI (Mueller et al., 2005) is the largest open-source AD study, providing longitudinal and multi-site neuroimaging data collected from 21 study sites. We utilized four AD-associated biomarkers from the ADNI dataset: (1) cortical thickness (CT) from MRI, (2) SUVR of Amyloid from PET, (3) SUVR of fluorodeoxyglucose (FDG) from PET, and (4) SUVR of Tau from PET. A total of 2153 subjects provided at least one MRI/PET image, with 1101 providing MRI for CT, 1205 providing Amyloid-PET, 1447 providing FDG-PET, and 549 providing Tau-PET. From the brain scans, we performed preprocessing to obtain brain regional measurements. We used the Destrieux atlas (Destrieux et al., 2010) to parcellate the cortical surface into 148 regions using T1-weighted MR images by skull stripping, tissue segmentation, and image registration. Based on the tissue segmentation result, we measured the average cortical thickness in each region by Freesurfer. For the Amyloid, FDG, and Tau, we calculated the region-wise average concentration level from PET scans. The cerebellum was used as the reference region to calculate the SUVR for each pathology modality.

Subsequently, we removed subjects whose age or label is missing and those who have only one time point. Consequently, we obtained 178, 687, 678, and 166 subject data for CT, Amyloid, FDG, and Tau respectively. The demographic details for these biomarkers are summarized in Table 4. The number of time points varies across subjects, with a minimum number of two for all biomarkers. The maximum number of time points is five for Amyloid, Tau, and CT, and ten for FDG. The average time interval between data collection points and their standard deviations are as follows:  $2.2 \pm 0.78$  years for CT,  $2.2 \pm 0.72$  years for Amyloid,  $1.3 \pm 1.20$  years for FDG, and  $1.2 \pm 0.37$  years for Tau.

The OASIS dataset (LaMontagne et al., 2019) provided Tau-PET scans from 81 subjects. To calculate regional Tau SUVR, we registered the PET scans to T1-weighted images and computed standard uptake values (SUV) for each region based on the Destrieux atlas. Similar to the ADNI preprocessing, we used the cerebellum as the reference region to compute the SUV ratio (SUVR). After excluding subjects whose age or label is missing and those with only a single time point, we retained 32 subjects. All subjects have two time points with a 6-month interval between data collection. Of the 32 subjects, three were diagnosed with AD; one had consistent AD diagnosis at both time points, while the other two transitioned from CN to AD. The demographic information for the OASIS dataset is presented in Table 5.

## B DETAILED IMPLEMENTATION SETTING

To train ConDOR, we used PyTorch with a single NVIDIA GeForce RTX 3090 GPU. For all biomarkers, we applied a stratified train-test split to the data, maintaining the ratio of the given five labels, with 80% of data used for training and the remaining 20% for testing. Also, for the multi-domain learning on Tau, we first combined the Tau datasets from ADNI and OASIS, and then applied a stratified train-test split to the unified dataset maintaining the sample size ratio of each domain. To prevent biased results, all experiments were replicated three times with different parameter initialization, and their average performance along with standard deviation were reported. In Table 6, we provide details of the implementation settings of ConDOR for all experiments on four biomarkers. We performed a grid search to choose the best learning rate in  $\{0.002, 0.0015, 0.001, 0.0008, 0.0005\}$ , and a batch size in  $\{16, 32\}$ . In the reverse process of RDM and TDM, U-Net (Ronneberger et al., 2015) is used to implement  $\epsilon_\theta(\cdot)$  and  $\epsilon_\phi(\cdot)$ . All codes will be released online after the review process.

Table 4: Demographics of the ADNI dataset. The numbers of subjects for each category were calculated based on the baseline time point samples. The number of records denotes the total number of cross-sectional samples across the population.

Biomarker	Category	CN	SMC	EMCI	LMCI	AD
Cortical Thickness	# of subjects	50	32	64	23	9
	# of records	112	72	152	56	39
	Gender (M / F)	26/24	24/8	40/24	13/10	5/4
	Age (Mean $\pm$ Std)	71.3 $\pm$ 4.2	72.1 $\pm$ 4.7	72.6 $\pm$ 6.9	74.2 $\pm$ 5.2	76.5 $\pm$ 7.1
Amyloid	# of subjects	150	87	238	158	54
	# of records	405	231	715	376	270
	Gender (M / F)	79/71	56/31	138/100	88/70	31/23
	Age (Mean $\pm$ Std)	71.9 $\pm$ 3.9	73.0 $\pm$ 4.9	73.3 $\pm$ 7.1	74.1 $\pm$ 7.9	76.0 $\pm$ 7.5
FDG	# of subjects	147	4	151	262	114
	# of records	415	4	345	966	580
	Gender (M / F)	82/65	3/1	94/57	167/95	67/47
	Age (Mean $\pm$ Std)	72.2 $\pm$ 3.5	73.9 $\pm$ 4.0	75.4 $\pm$ 5.8	76.6 $\pm$ 6.9	77.2 $\pm$ 6.5
Tau	# of subjects	30	37	48	31	20
	# of records	65	85	118	76	55
	Gender (M / F)	28/37	25/60	66/52	44/32	26/29
	Age (Mean $\pm$ Std)	68.4 $\pm$ 3.7	68.9 $\pm$ 3.8	69.8 $\pm$ 5.9	71.0 $\pm$ 7.4	78.8 $\pm$ 8.4

Table 5: Demographics of the OASIS dataset. The numbers of subjects for each category were calculated based on the baseline time point samples. The number of records denotes the total number of cross-sectional samples across the population.

Biomarker	Category	CN	AD
Tau	# of subjects	31	1
	# of records	60	4
	Gender (M / F)	13/18	1/0
	Age (Mean $\pm$ Std)	63.2 $\pm$ 7.5	71.9 $\pm$ 1.6

Table 6: Hyperparameters of CondOR for all experiments.

	Hyperparameter	CT	Amyloid	FDG	Tau
Train	Optimizer	Adam	Adam	Adam	Adam
	Learning rate	0.001	0.001	0.0008	0.0008
	Learning rate scheduler	MultiplicativeLR	MultiplicativeLR	MultiplicativeLR	MultiplicativeLR
	Learning rate decay	0.999	0.999	0.999	0.999
	Batch size	16	16	16	16
	Number of epochs	10000	10000	10000	10000
KDE	bandwidth $h_b$	0.001	0.001	0.001	0.001
$\epsilon_\theta$	Hidden dimension	64	64	64	64
	Number of layers	4	4	4	4
	Number of initial channel	1	1	1	1
	Number of hidden channels	[64, 128, 256, 512]	[64, 128, 256, 512]	[64, 128, 256, 512]	[64, 128, 256, 512]
	Number of final channels	1	1	1	1
	Number of sampling steps	1000	1000	1000	1000
$\epsilon_\phi$	Hidden dimension	64	64	64	64
	Number of layers	4	4	4	4
	Number of initial channel	1	1	1	1
	Number of hidden channels	[64, 128, 256, 512]	[64, 128, 256, 512]	[64, 128, 256, 512]	[64, 128, 256, 512]
	Number of final channels	1	1	1	1
	Number of sampling steps	100	100	100	100
	cohort-level weight $\lambda$	0.1	0.1	0.1	0.7

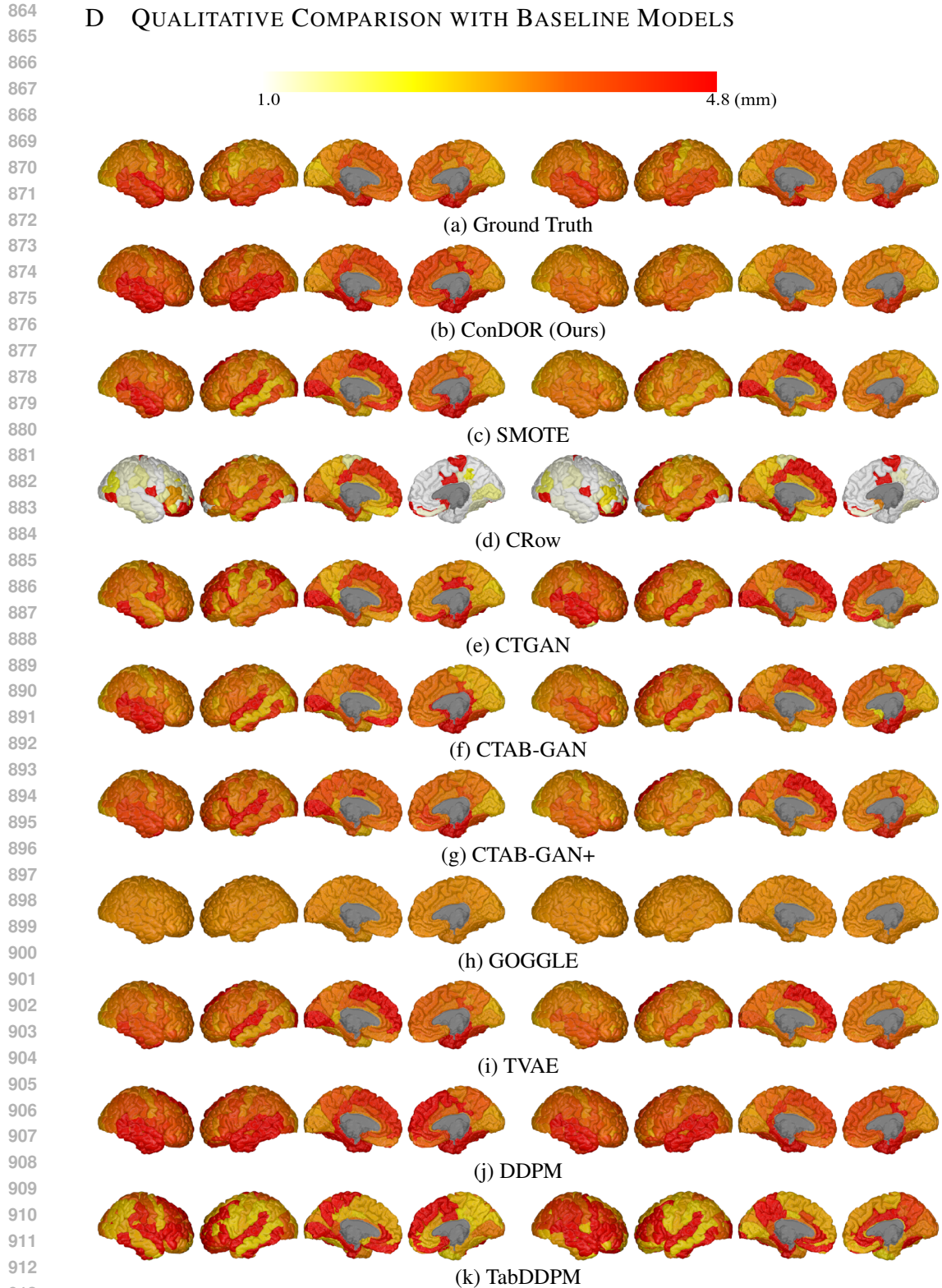
## C LIMITATION AND FUTURE WORK

**Limitations.** (1) Compared to one-shot generative methods such as TVAE and GANs, our autoregressive approach has a longer generation time since samples are generated sequentially. The gap in the sampling time becomes significantly larger as the sequence length (i.e., the number of time points) becomes extended. (2) Additionally, our method may face challenges in scenarios where labels are abruptly reversed over time. In such cases, the interpolated label  $y_t^d$  may not represent a feasible disease severity and could deviate from the range of given observed labels, which may highly likely aggravate the training stability and model performance. In our experiments, we confirmed that all sequence labels are monotonically deteriorating, so the  $y_t^d$  in equation 10 is defined under the strict assumption of ordinal transitions. (3) The four AD biomarkers used in the experiments (i.e., cortical thickness, SUVR of Amyloid, FDG, and Tau) are widely recognized and clinically validated biomarkers for identifying AD (Querbes et al., 2009; Jack & Holtzman, 2013). However, these biomarkers may not fully represent the broader spectrum of neurodegenerative diseases, such as Parkinson’s or Huntington’s disease, which involve different biological mechanisms. Additionally, the AD datasets utilized in our experiments primarily consist of participants from the US, potentially limiting the model’s applicability to populations with different genetic, environmental, or lifestyle factors. This lack of population diversity could affect the generalizability of the findings across broader demographics.

**Future Works.** (1) While the dual-sampling approach in our method effectively balances both cohort and subject-level information, it may introduce biased results if the trade-off hyperparameter  $\lambda$  is not appropriately tuned. The ablation studies on the  $\lambda$  in Table 3 indicate that the bias is not critical in general. However, considering the inefficiency of fine-tuning for every dataset, we plan to develop adaptive mechanisms that dynamically adjust the  $\lambda$  based on dataset characteristics, ensuring optimal balance between cohort and subject-level contributions. (2) Moreover, we plan to extend our model by incorporating additional AD-relevant conditions, such as blood plasma (Schneider et al., 2009; Hansson et al., 2023). Along with the age and diagnostic labels, this biomarker could be utilized as time-dependent conditions and could provide complementary information to understand AD progression, ultimately enhancing the biological plausibility and robustness of the generated data.



## D QUALITATIVE COMPARISON WITH BASELINE MODELS



913 Figure 4: Example of ground truth and generated results from the CT experiment. This subject  
 914 (ID: 029\_S\_4385) has two time points with age/label 68.2/CN at the first time point and 71.8/AD at  
 915 the second time point. Each set, consisting of the outer right, outer left, inner left, and inner right  
 916 hemispheres, shows the results from one time point, with time points increasing from left to right.  
 917

918  
 919  
 920  
 921  
 922  
 923  
 924  
 925  
 926  
 927  
 928  
 929  
 930  
 931  
 932  
 933  
 934  
 935  
 936  
 937  
 938  
 939  
 940  
 941  
 942  
 943  
 944  
 945  
 946  
 947  
 948  
 949  
 950  
 951  
 952  
 953  
 954  
 955  
 956  
 957  
 958  
 959  
 960  
 961  
 962  
 963  
 964  
 965  
 966  
 967  
 968  
 969  
 970  
 971

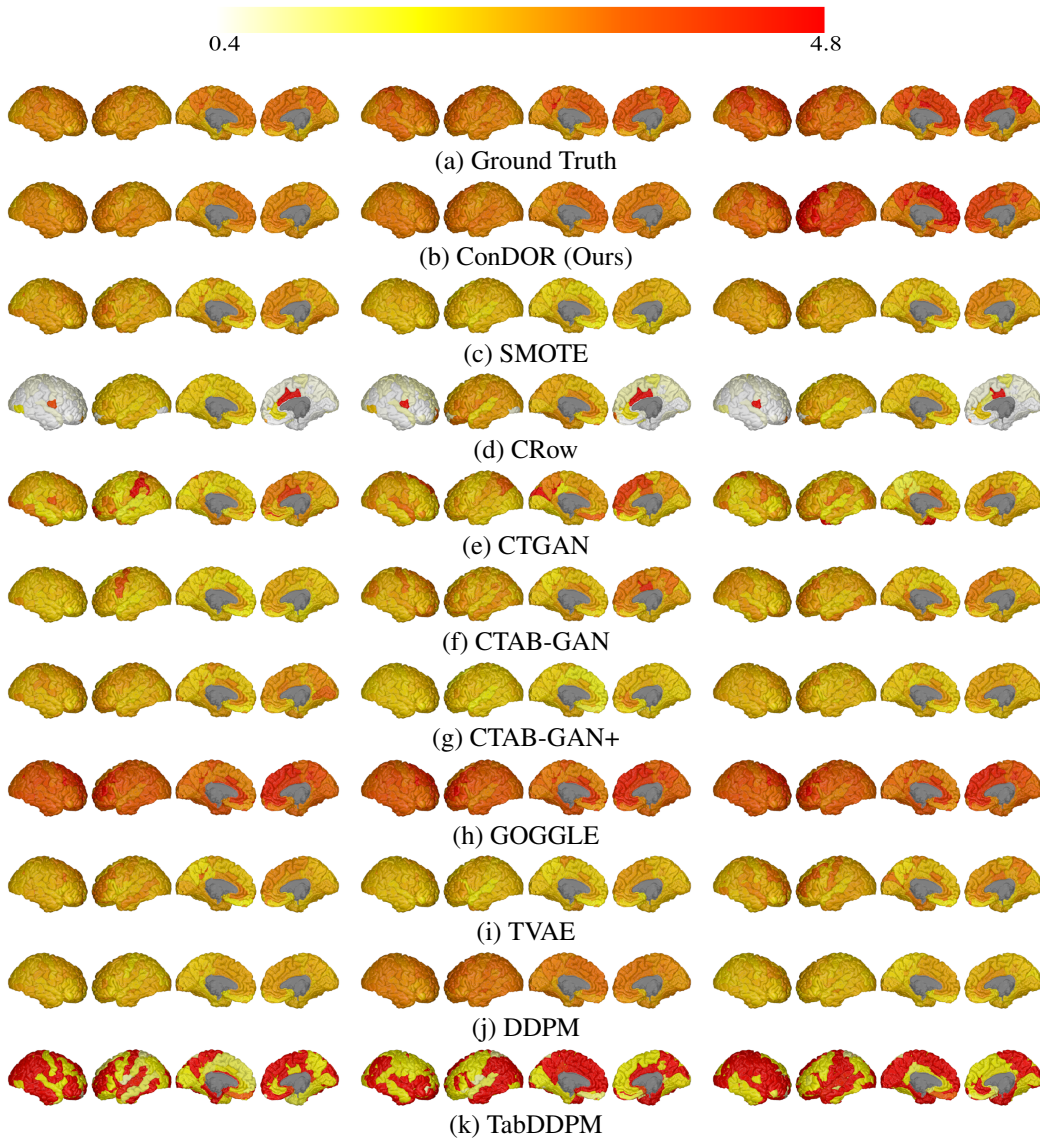


Figure 5: Example of ground truth and generated results from the Amyloid experiment. This subject (ID: 127\_S\_2213) has three time points with age/label 82.3/EMCI at the first time point, 84.3/EMCI at the second time point, and 86.3/EMCI at the third time point. Each set, consisting of the outer right, outer left, inner left, and inner right hemispheres, shows the results from one time point, with time points increasing from left to right.

972  
973  
974  
975  
976  
977  
978  
979  
980  
981  
982  
983  
984  
985  
986  
987  
988  
989  
990  
991  
992  
993  
994  
995  
996  
997  
998  
999  
1000  
1001  
1002  
1003  
1004  
1005  
1006  
1007  
1008  
1009  
1010  
1011  
1012  
1013  
1014  
1015  
1016  
1017  
1018  
1019  
1020  
1021  
1022  
1023  
1024  
1025

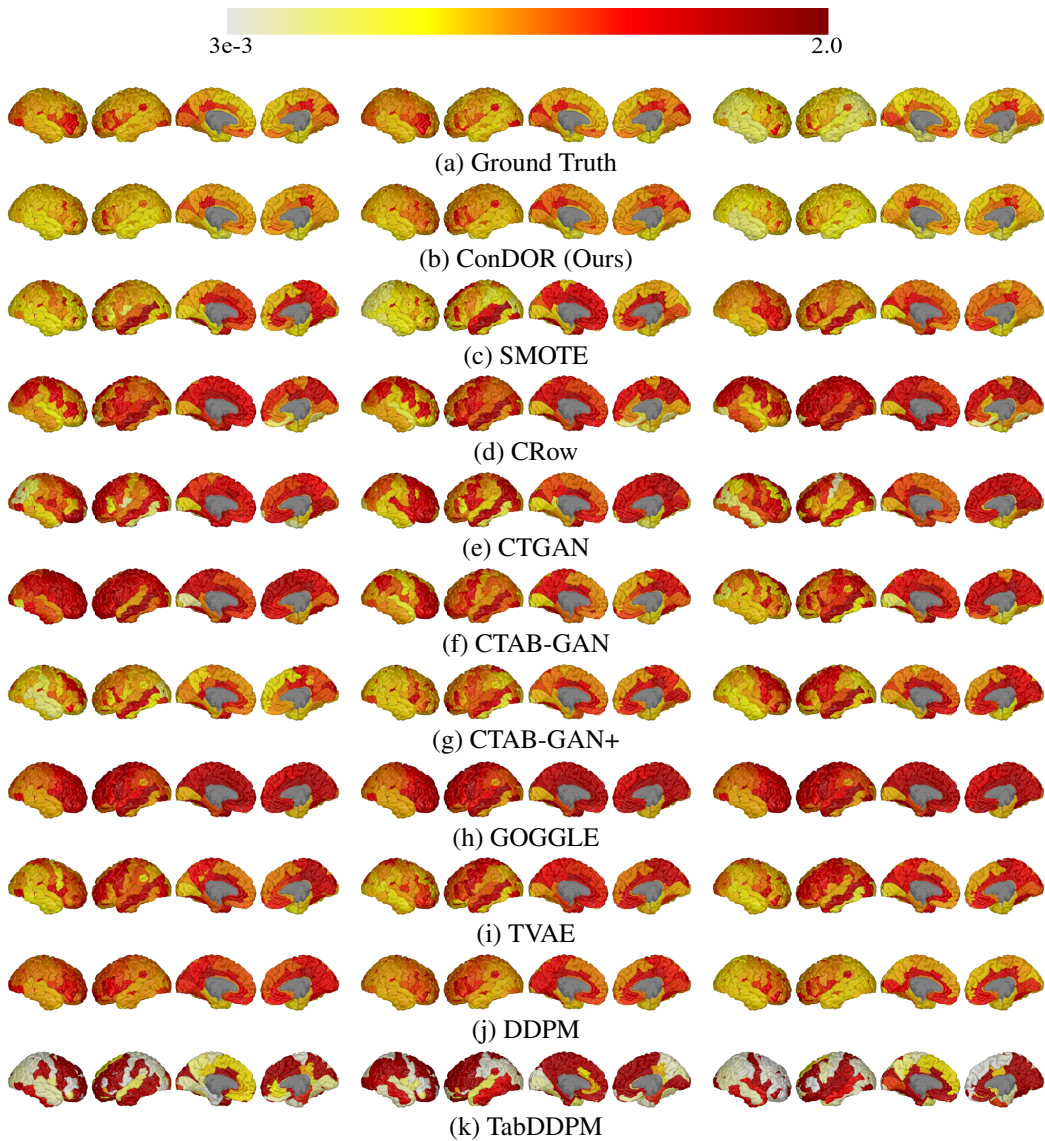


Figure 6: Example of ground truth and generated results from the FDG experiment. This subject (ID: 037\_S\_1078) has three time points with age/label 70.6/LMCI at the first time point, 72.3/LMCI at the second time point, and 75.6/AD at the third time point. Each set, consisting of the outer right, outer left, inner left, and inner right hemispheres, shows the results from one time point, with time points increasing from left to right.

1026  
 1027  
 1028  
 1029  
 1030  
 1031  
 1032  
 1033  
 1034  
 1035  
 1036  
 1037  
 1038  
 1039  
 1040  
 1041  
 1042  
 1043  
 1044  
 1045  
 1046  
 1047  
 1048  
 1049  
 1050  
 1051  
 1052  
 1053  
 1054  
 1055  
 1056  
 1057  
 1058  
 1059  
 1060  
 1061  
 1062  
 1063  
 1064  
 1065  
 1066  
 1067  
 1068  
 1069  
 1070  
 1071  
 1072  
 1073  
 1074  
 1075  
 1076  
 1077  
 1078  
 1079

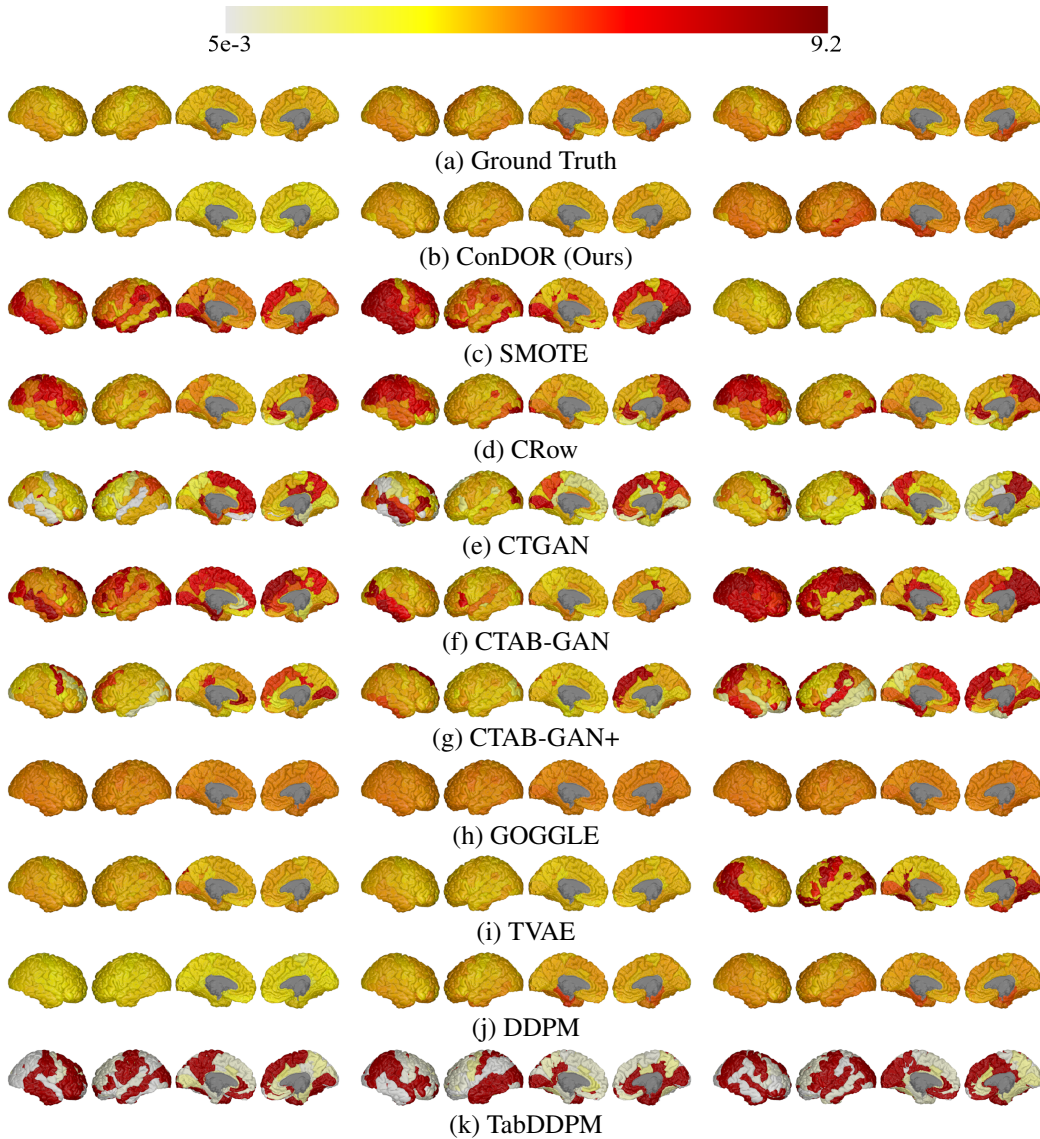


Figure 7: Example of ground truth and generated results from the ADNI dataset on Tau experiment. This subject (ID: 023\_S\_1190) has three time points with age/label 76.5/EMCI at the first time point, 78.0/AD at the second time point, and 79.3/AD at the third time point. Each set, consisting of the outer right, outer left, inner left, and inner right hemispheres, shows the results from one time point, with time points increasing from left to right.

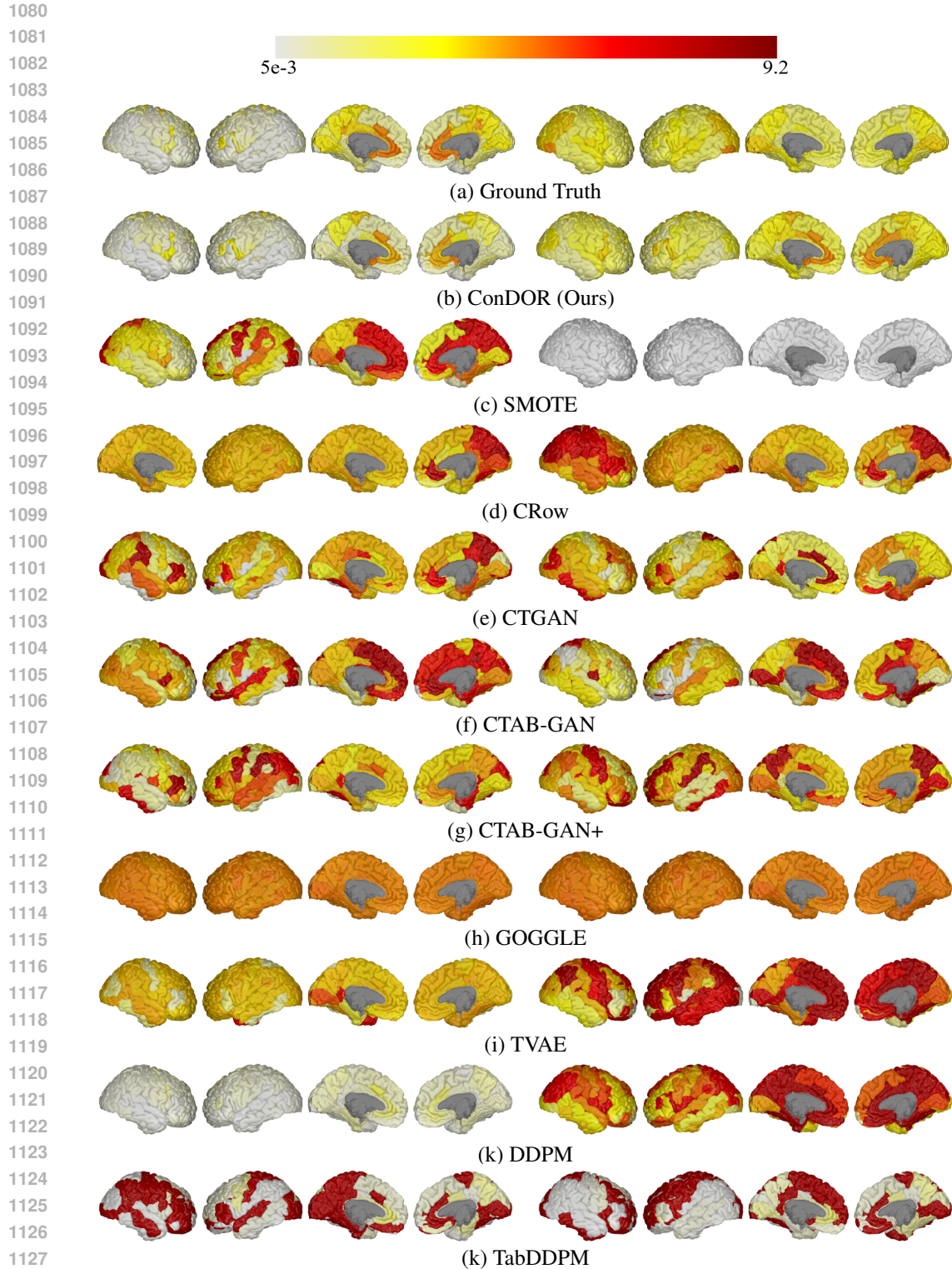


Figure 8: Example of ground truth and generated results from the OASIS dataset on the Tau experiment. This subject (ID: OAS30818) has two time points with age/label 70.0/CN at the first time point and 70.5/AD at the second time point. Each set, consisting of the outer right, outer left, inner left, and inner right hemispheres, shows the results from one time point, with time points increasing from left to right.

1134 E ADDITIONAL QUALITATIVE RESULTS: A VIDEO SHOWING 20-YEAR  
1135 CHANGES IN AMYLOID SUVR  
1136

1137 In the supplementary material, we provide a video showcasing qualitative results from ConDOR on  
1138 Amyloid SUVR, illustrating the sequential changes of a subject aged 65 to 85, with five diagnostic  
1139 labels transitioning from CN to AD. Considering the baseline age distributions of the five labels  
1140 used in the Amyloid experiment (Table 4), the age range from 65 to 85 appropriately aligns with  
1141 the real-world longitudinal samples labeled from CN to AD. The video illustrates that the Amy-  
1142 loid SUVR of the generated sample generally increases as the disease worsens. These results are  
1143 consistent with the established patterns of Amyloid accumulation observed in Alzheimer’s disease,  
1144 demonstrating the effectiveness of ConDOR in capturing the dynamics of the biomarker along the  
1145 disease progression.

1146  
1147  
1148  
1149  
1150  
1151  
1152  
1153  
1154  
1155  
1156  
1157  
1158  
1159  
1160  
1161  
1162  
1163  
1164  
1165  
1166  
1167  
1168  
1169  
1170  
1171  
1172  
1173  
1174  
1175  
1176  
1177  
1178  
1179  
1180  
1181  
1182  
1183  
1184  
1185  
1186  
1187